Microcrack characterization of loaded Engineered Cementitious Composites via optical scans and photogrammetric analyses

Duo Zhang, Wentao Wang [*], Victor C. Li

Department of Civil and Environmental Engineering, University of Michigan
2350 Hayward Street, Ann Arbor, MI 48109, United States

ARTICLE INFO

ABSTRACT

Concrete cracks accelerate the ingress of harmful species and must be gauged accurately for durability evaluation and prediction. As a novel class of ultra-ductile concrete, Engineered Cementitious Composites (ECC) develops multiple sub-hairline cracks that are difficult to visualize using conventional techniques. In this study, a semi in-situ laboratory approach is proposed based on optical microscopy and photogrammetric analysis to enhance the accuracy of crack width measurement in ECC. Microscopic images scanned from the material surface were reconstructed and analyzed to extract the statistics of crack width, location, number, and spacing. Results suggested that general portable microscopes can effectively identify cracks smaller than 2 μm in loaded condition and provide magnified high-resolution crack images that are hardly achieved by regular digital cameras. Crack openings can be isolated via 2D FFT filtering and binarized to attain the datasets of crack spacing and crack width distribution. In contrast to microscopy, conventional digital image correlation (DIC) as an indirect method was found to overestimate sub-pixel crack widths particularly when the crack width and spacing are substantially smaller than the image resolution. In these scenarios, it is recommended to combine optical microscopy with DIC to ensure simultaneously accurate and holistic crack width characterization. The proposed technique can be used for general materials with multiple fine cracks.

1. Introduction

As a typical brittle material, concrete is subjected to uncontrolled cracking at the material level. The literature shows that a broad spectrum of concrete durability indicators, such as permeability [1], chloride diffusion [2], and steel rebar corrosion [3], is strongly correlated to the crack width. Large crack widths provide easy pathways for the ingress of harmful species, thus accelerating structural degradation. Therefore, accurate measurement of crack width and understanding the crack opening process are critical for assessing material properties, enhancing performance, and predicting durability.

Engineered Cementitious Composites (ECC) is a novel class of fiber-reinforced cementitious composites (FRCC) featuring ultra-high tensile ductility and strain-hardening characteristics [4]. Unlike conventional brittle concrete, ECC is designed with a built-in material property to control its crack width and shows a typical tensile strain capacity higher than 3%, i.e., 300 times that of conventional concrete [5–7]. The tailored microfiber bridging enables ECC to carry loads even after cracking while allowing additional micro-cracks to form and subsequently saturate along the loading direction. The crack width stabilizes at 30–100 μm irrespective of the imposed loads/strains [8]. Fig. 1 shows a typical ECC stress–strain relationship and the crack width development in tension [9]. The tight crack width drastically reduces permeability [1] and facilitates self-healing [10–12], thus mitigating the need for repeated repair and maintenance. By coupling durable binders and robust microfiber reinforcement, the intrinsically tight cracks in ECC provide a potential avenue to enhance concrete durability drastically.

The multiple fine cracking in ECC presents a unique challenge for measuring the crack number and width. Traditional concrete measuring tools, such as crack gauge/comparator, measure cracks larger than 100 μm and do not satisfy the need for high resolutions in ECC. The cracks of ECC in loaded condition differ from the residual cracks after releasing the load due to the partial crack closure led by the material relaxation [13] and therefore should be measured before unloading to emulate field conditions. To approximate the average crack width in loaded condition, previous studies [14,15] divided the specimen gauge length elongation by the number of cracks, assuming that the material

Fig. 1. Typical tensile stress/strain relationship and crack width evolution of ECC.

2. Experimental program

2.1. Specimen preparation

Materials used in this study include Type I Portland cement, Class C fly ash, metakaolin, limestone powder, and PVA fibers (RECS15, Nycon). A high-range water reducer was used. The geometry and physical properties of PVA fibers are listed in Table 1. Two proprietary PVA-ECC formulations were used with/without the incorporation of crumb rubber. Specific mix designs and mixing/casting protocols will be disclosed separately. As the present study focuses on the procedure of crack width measurement, the absence of mix designs does not influence the data interpretation and conclusions of this paper.

The fresh mixtures were cast into dogbone-shaped specimens with the dimensions illustrated in Fig. 2. The specimens were demolded after 1 day and were subsequently cured for 180 days in air condition. Before testing, the specimens were painted in white to enhance the contrast between crack opening and non-cracked background, and were then speckled in red for DIC analysis. The random speckles also create unique features of each microscopic image that enhance the accuracy of image stitching. Conventional black speckles used for DIC exhibit color features close to crack openings, thus complicating the image analysis for crack identification. Based on a set of experimental trials, red speckles were chosen to differentiate the RGB feature and isolate speckles from cracks, which meet the requirements of both DIC and optical microscopy. Fig. 3 shows the ECC specimen in its white-painted and red-speckled conditions.

2.2. System design and setup

To maneuver the view of the microscope, a computer-controlled automatic setup was developed for attachment to a bench-top Instron loading system. As shown in Figs. 4 and 5, the setup comprises a stepper motor equipped with a linear actuator, a guiding rail, an aluminum frame, and a 3-MP microscope camera (AMScope, MD300). The stepper motor was controlled by a LabVIEW program that defines the start/end location, speed, and step size of the microscope's vertical movement. The microscope was fixed horizontally.

The microscope's traveling distance was set as 40 mm along the specimen's centerline in the loading direction. To ensure that all microscopic images can be stitched properly, each view was captured at least twice at a 0.5-mm step size, thus producing approximately 160 images for each scan. The residence time, i.e., the time interval between each step, was set as 10 s. All images were taken at a $40 \times$ magnification by the optical microscope and were saved in 2048×1536 pixels. The pixel size was calibrated as 0.6 μm. Note that the microscope pixel size can be adjusted further down to 0.3 μm by saving as high-resolution images.

A 24-MP Canon Mark II digital camera was used to capture the entire gauge length (i.e., 40 mm). As shown in Fig. 5, the microscope and digital camera were set on the same side of the loading frame, and therefore only one side of each specimen was examined. As the microscope has a smaller working distance than the digital camera, it was placed between the specimen and the digital camera lens and was designed to turn 90° clockwise/counter-clockwise to expose the entire loaded section for DIC image collection. The DIC image resolution was calibrated at approximately 30 μm.

elongation is exclusively attributed to crack openings and the elastic elongation of uncracked materials is negligible. The number of cracks is mostly counted from digital images or directly from visual inspection. This method can be easily applied before/after unloading, but fails to provide detailed information on the crack width distribution, i.e., histograms of the numbers of cracks in various width intervals. Adding up individual cracks could also be time-consuming and may produce arbitrary results regarding ultra-fine and discontinuous cracks.

Techniques based on photogrammetry have been adopted for in-situ crack measurements in concrete/ECC. In laboratory practices, digital cameras are used to capture the specimen surface during loading and the images are analyzed onsite/offsite to determine crack widths based on the calibrated pixel size. Among these methods, digital image correlation (DIC) [16–18] proves to be efficient by providing 2D/3D strain fields from the deformation of predefined subsets [19,20]. The subsets are groups of surface objects that contain unique speckle features and can be located on images of a constant area of interest before and after deformation. The DIC-calculated strain field can be used to locate surface strain concentrations associated with cracks and to determine crack widths through strain integration. Despite the easiness of operation, DIC is reportedly prone to computational errors due to the heterogeneity of cracked materials and may lead to unreliable strain values adjacent to cracks [16,17]. Apart from DIC, the accuracy of crack width measurement by photogrammetry is governed by the resolution limit of regular digital cameras. Depending on the working distance and camera type, digital images have resolutions varying from 10 to 50 μm in most laboratory configurations [21], which is insufficient to cover all ranges of crack width possibly found in ECC. Prior studies [22,23] applied counter-top optical microscopes to measure ECC's crack width while locking the specimen to selected strains for permeability tests. Although a high accuracy can be achieved, it is an off-site method and unable to continue loading and measuring the same specimen at higher strain levels.

The present study proposes a lab-scale microscopic photogrammetric approach that measures crack width at high resolutions on the same specimen loaded to varying tensile strains. A custom setup equipped with a portable optical microscope is developed to conduct surface line scanning while holding the specimen at selected strains. The procedure of the photogrammetric analysis including microscopic image-stitching, frequency-domain de-noising, and image binarizing is developed. Conventional DIC is conducted as control. As a (semi) in-situ technique, the proposed approach allows direct measurements of crack width, location, and spacing, and satisfies the resolution need for measuring microcracks of all width ranges in ECC.

Table 1
PVA fiber properties.

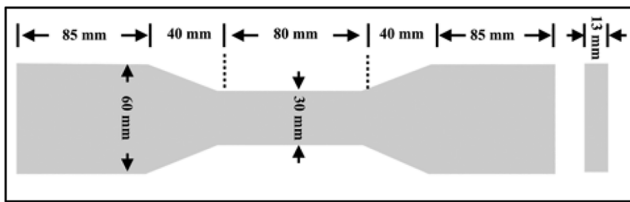| Length, mm	Diameter, μm	Elongation, %	Density, kg/m^3	Young's modulus, GPa	Tensile strength, MPa
8	39	6	1300	42.8	1600

Fig. 2. ECC specimen dimensions.

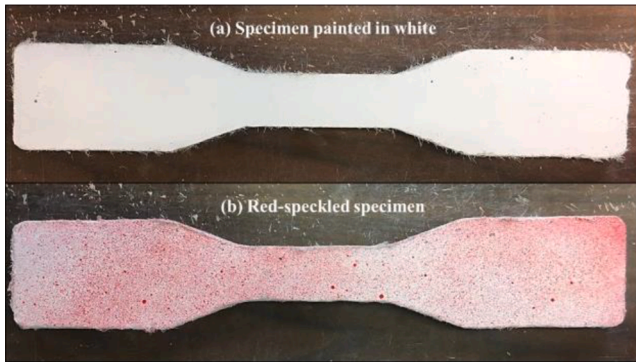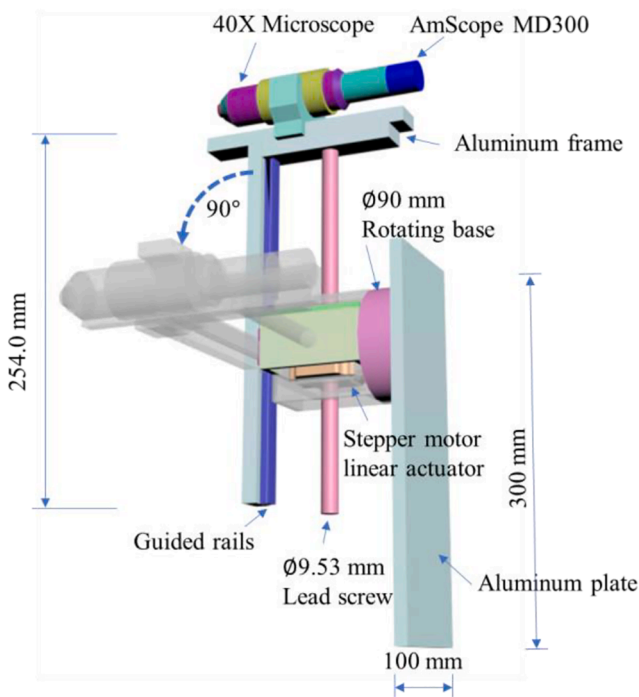**Fig. 3.** ECC specimen, (a) painted in white, and (b) randomly speckled in red.

Fig. 4. Design of microscope setup for line scanning.

Fig. 5. Loading and testing setup.

2.3. Loading and image acquisition

The ECC specimens were tested under a uniaxial tension configuration as shown in Figs. 5 and 6. To track the specimen tensile strain, a pair of LVDT with a 40-mm gauge length was used to collect the elongation every second. The loading process followed a displacement-controlled program at a constant rate of 0.5 mm/min. The Instron system was able to pause the load at selected tensile strains while holding the specimen under the loaded status. The specimen tensile strains calculated from the real-time LVDT readings were used to inform manual
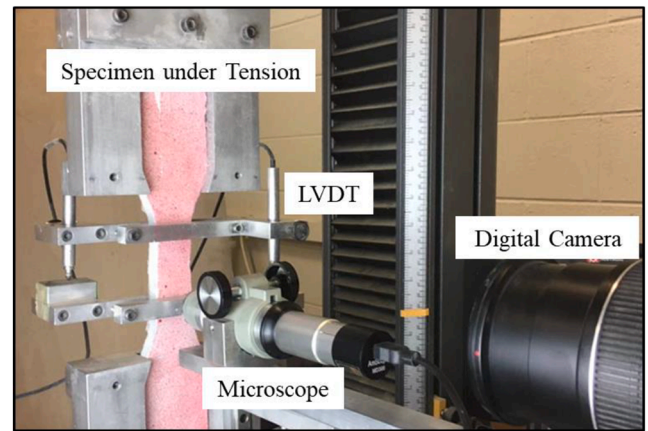
operations of pausing/resuming the load.

The testing protocol is graphically illustrated in Fig. 6. For each specimen, images of the entire loaded section were collected sequentially during the loading ramp, while microscope scans were conducted when the load paused at selected strain levels. For specimens examined in this study, the paused tensile strains were chosen at 0.5%, 1% and 2% followed by a 1% increment until ultimate failure. As shown in Fig. 6, the testing procedure comprises 4 steps: 1) load the specimen to the first selected strain, i.e., 0.5% (as indicated by LVDT readings) while collecting sequential images of the entire gauge length, i.e., 40 mm; 2) pause the load and digital camera, and hold the specimen under the strain level. This step may incur stress relaxation as fibers were slowly slipped off from the matrix during the holding time (see Fig. 7). This impact on crack widths was estimated by the change of LVDT readings during the holding time and was found to be negligible compared to the actual crack width. Therefore, its influence on crack width was not taken into consideration; 3) scan cracks along the specimen centerline from bottom to top; and 4) resume loading and digital image collection and repeat Steps 2–3 to complete the microscope scans at all selected strains. The tensile stress–strain relationships are shown in Fig. 7, and typical views of the microscope and digital camera are shown in Fig. 8. Both specimens exhibited distinct tensile strain-hardening characteristics and high strain capacities up to 2% for Specimen A and 5.5% for Specimen B.

3. Microscopic image processing and analysis

3.1. Raw image processing and binary conversion

Before analyzing crack information, the microscopic images were processed to enhance the contrast between the cracks and cementitious background. The procedure is described in Fig. 9. The raw sequential images were stitched across the entire section in the longitudinal direction and were converted to the RGB format that translates to a 3-dimensional array, i.e., the first/second dimensions defining pixel location and the third dimension defining red, green and blue levels (0–255). It was then converted to a grayscale image defined by its red level to filter off the red speckles. As shown in Fig. 9, the remaining objects on the grayscale image are attributed to cracks and minor noises, which, however, exhibit overlapping grayscale intensities that are not able to be separated by the color feature. These objects will be analyzed regarding their frequency feature [24,25].

To isolate cracks from random sparse noises, the fast Fourier transform (FFT) is used to determine the frequency domain of the grayscale image, thus defining a bandpass spectrum that separates objects of different frequencies. FFT has been often used for signal processing and data analysis to enhance the signal-to-noise ratio. Performing FFT in two directions, i.e., two-dimensional fast Fourier transform (2D-FFT), can
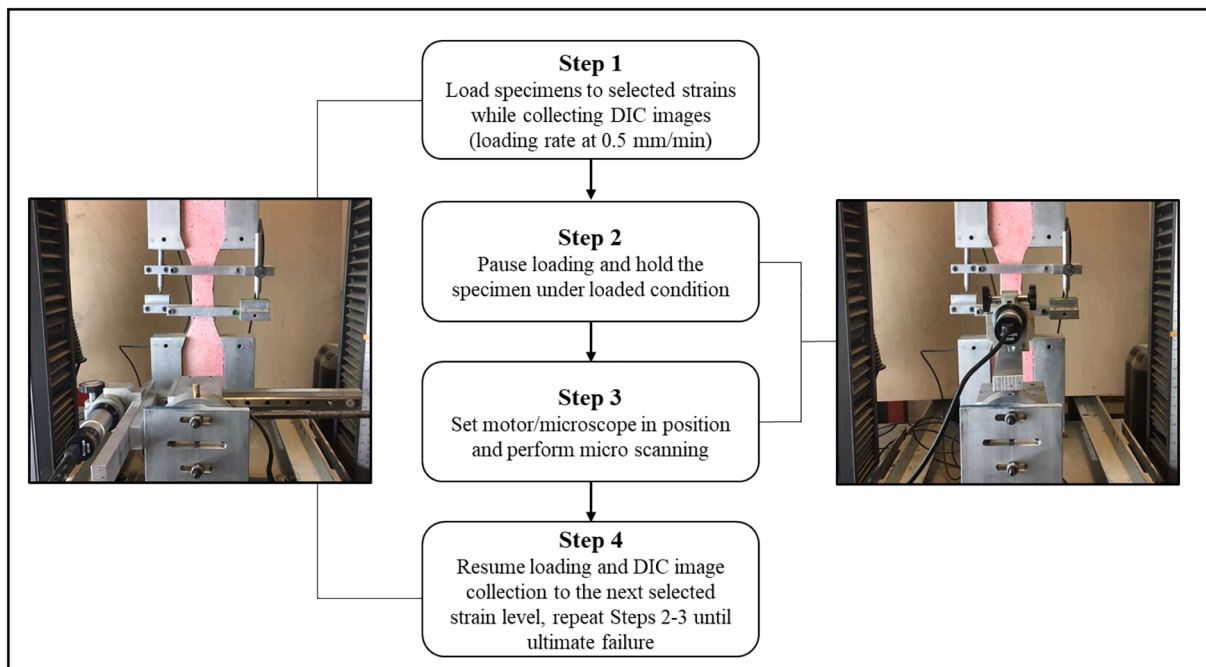
Fig. 6. Testing and image acquisition procedure.

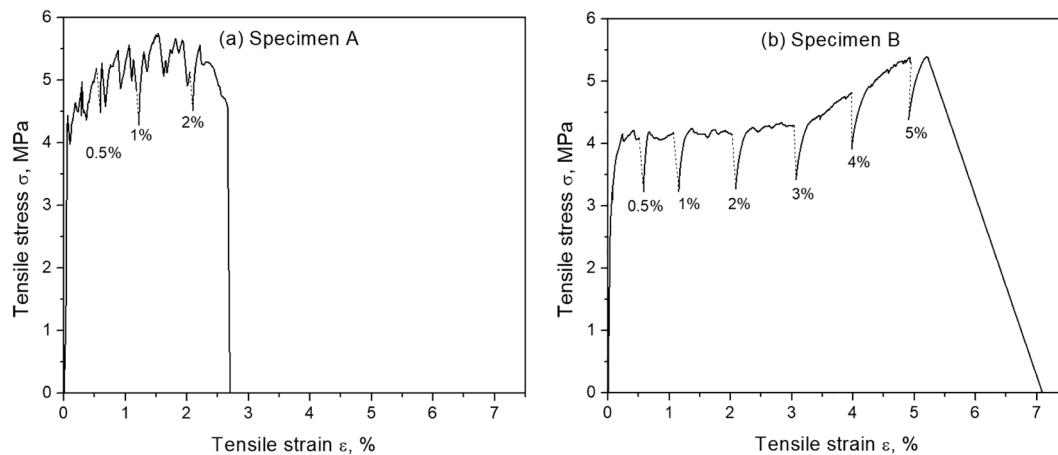**Fig. 7.** Tensile stress/strain relationship, (a) Specimen A, and (b) Specimen B. The inserted tensile strains are approximated based on LVDT readings Fig. 7. Tensile stress/strain relationship, (a) Specimen A, and (b) Specimen B. The inserted tensile strains are approximated based on LVDT readings.
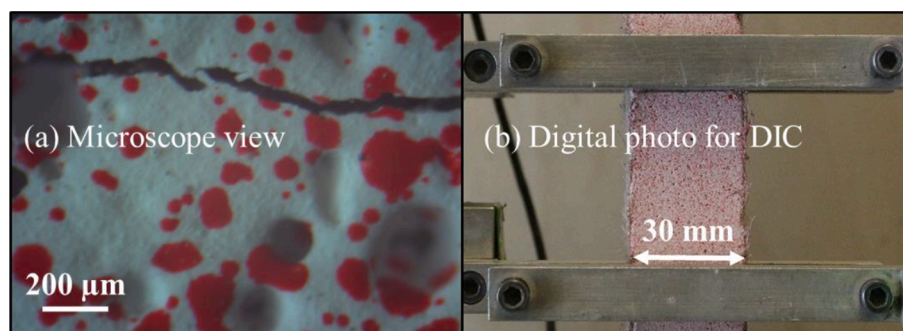

Fig. 8. Typical views of (a) single microscope image, and (b) digital camera image for DIC.

assist in distinguishing between cracks and noises, which differ substantially from each other in the frequency domain in both longitudinal and transverse directions. The transform and bandpass spectrums were obtained as global parameters from the stitched image and are depicted in Fig. 9 for a typical 5-mm long section. The bandpass spectrum was defined to filter off objects of high frequencies (i.e., pores/voids) and
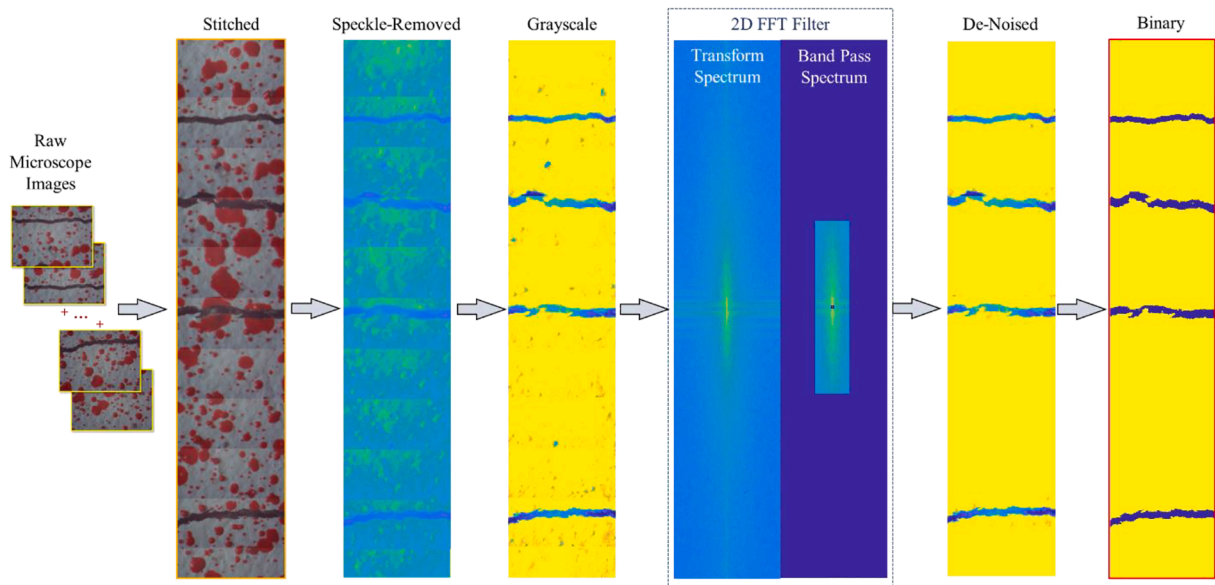
Fig. 9. Microscope image processing of a 5-mm long section.

low frequencies (i.e., noises), leaving medium frequency objects (i.e., cracks) as shown in the de-noised image [26]. Note that for consistent crack measurement, it is important to process the 2D-FFT treatment on the stitched panoramic images rather than individuals. The former is necessary to establish a global bandpass spectrum based on the entire section. After de-noising, the grayscale image can be turned into a binary image in which objects are exclusively attributed to cracks as shown in Fig. 9.

3.2. Image de-noising in frequency domain

The 2D-FFT process for the de-noising treatment is detailed in this section. Instead of transferring one-dimensional signals of temporal variations, the microscopic images are typical two-dimensional matrices that represent intensity variations in the spatial domain. After resampling and stitching, the image length N and width M are 3,126 and 626 in pixel, representing 5 mm and 1 mm, respectively. The grayscale image can be converted between the matrix form and the frequency domain using the discrete 2D-FFT given in Eqs. (1–2).

$$F(u,v) = \frac{1}{MN} \sum_{x=0}^{M-1} \sum_{y=0}^{N-1} f(x,y) e^{-j2\pi\left(\frac{ux}{M}+\frac{vy}{N}\right)} \tag{1}$$

$$f(x,y) = \sum_{u=0}^{M-1} \sum_{v=0}^{N-1} F(u,v) e^{j2\pi\left(\frac{ux}{M}+\frac{vy}{N}\right)} \tag{2}$$

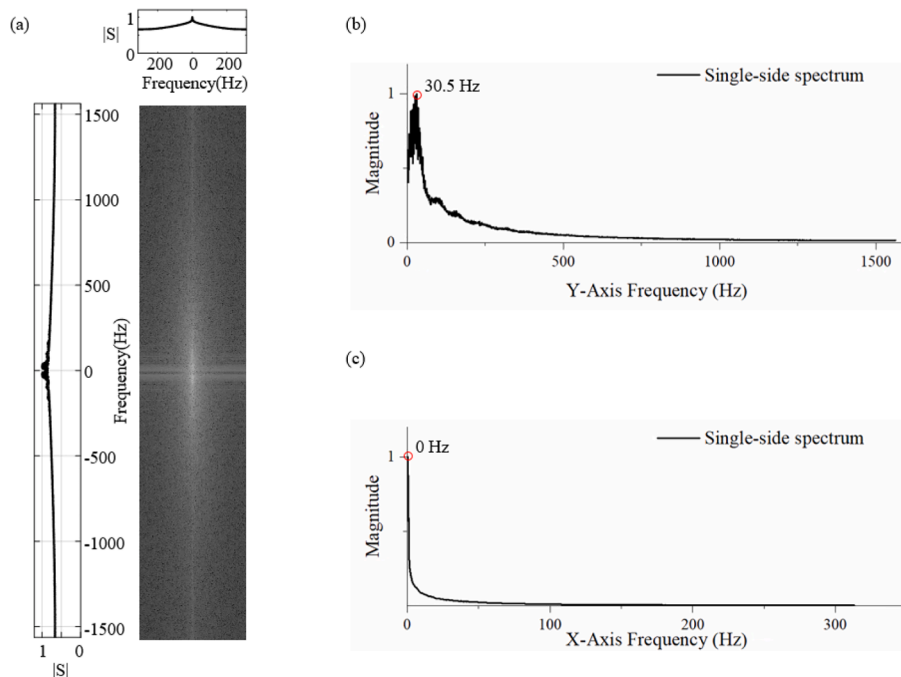where $F(u,v)$ is the FFT coefficient in the two-dimensional discrete fre-

Fig. 10. Spectrum characteristics of the cracks (a) 2D-FFT and the two-side power spectral representations of the grayscale image of the stitched microscope image; (b) single-side spectrum along *y*-axis; (c) single-side spectrum along *x*-axis.

quency domain (i.e., the u and v dimensions, $0 \leq u \leq M-1$ and $0 \leq v \leq N-1$), $f(x, y)$ is the inverse FFT coefficient in the $\times$ and y directions, and $j = \sqrt{-1}$ is the imaginary unit. An image of $M \times N$ pixels has an $M \times N$ set of (complex) FFT and inverse FFT coefficients. In the image processing, Eq. (1) is used to transform the grayscale image into the frequency domain. The image is de-noised in the frequency domain and is subsequently transformed back to grayscale using Eq. (2) [27].

Fig. 10 shows the 2D-FFT pattern and its power spectral representations in x-axis ($N = 626$ pixels) and y-axis ($M = 3126$ pixels). The frequency of the output coefficient matrix 2D-FFT, $F(u, v)$, represents the periodic performance of the image characteristics. 2D-FFT decomposes an arbitrary signal into a combination of sinusoidal signals whose magnitudes are given in the real part of the $F(u, v)$ matrix and frequencies are displayed along the x and y axes [28]. As shown in Fig. 10a, the frequency spectrum displays symmetric feature about the x and y axes. Each quadrant is mirrored from the adjacent quadrant with symmetric real part (i.e., magnitude) and imaginary part (i.e., phase). Fig. 10b and c show the frequency spectrum in the positive directions of the y-axis and x-axis, respectively. The sampled frequency range is chosen to be the same as the number of pixels, i.e., 0–1563 Hz for y-axis and 0–313 Hz for x-axis, according to the Nyquist–Shannon sampling theorem. The sharp peak around 30.5 Hz in Fig. 10b indicates the most significant crack width to be $3126/(2 \times 30.5) = 51.25$ pixels $\approx 62\mu$ m. Along the x-axis, the spectrum peak was found at 0 Hz, suggesting that the sample surface is dominated by continuous cracks throughout the x-direction. This is consistent with the visual inspection of the raw stitched image as shown in Fig. 9.

After transforming the image from grayscale into the frequency domain, a bandpass filter was proposed to isolate cracks from noises. The bandpass filters are equiradial 4th order lowpass Butterworth filters with lower and upper cut-off frequencies defined in both x and y directions. To guide the selection of the cutoff frequencies, Fig. 11 illustrates the effect of the frequency range on the result of crack number. As shown in Fig. 11, the lower and upper frequencies are chosen to vary in 5–60 Hz and 80–3100 Hz, respectively. At Point A with a cutoff frequency range of 5–80 Hz, the de-noised image displayed 4 cracks after filtering. By increasing the upper frequency to 3120 Hz, i.e., Point B, the image displays additional noises that lead to an overestimated number of cracks. Increasing the lower cut-off frequency, however, tends to filter

off the pixels that originally belong to cracks. Consequently, a single crack may be mistaken as multiple ones along the x-direction as exemplified by Point C. Note that Points C and D have the cut-off frequency ranges of 60–3100 Hz and 60–80 Hz, respectively, which exclude the typical crack frequency, i.e., 30.5 Hz (as indicated by the peak location in Fig. 10b), thus leading to the contraction and discontinuity of the crack objects. It suggests that the peak frequency must be included in the bandpass range to ensure the accuracy of the cracks width evaluation. In this study, the cut-off frequency ranges are chosen as 20–1000 Hz in the y-direction and 20–200 Hz in the x-direction.

This image processing approach was applied to all microscopic images. Figs. 12 and 13 displayed typical 5-mm long sections for Specimen A and Specimen B, respectively, where the micro-cracks can be clearly visualized on the binary images. The crack width appeared to be larger on Specimen A than B even at lower tensile strains. The shapes of cracks on Specimen B were found to be relatively tortuous and less connective. As shown in Fig. 13, Specimen B developed ultrafine cracks that were mostly indiscernible from the raw images, especially at the 5% tensile strain.

3.3. Crack analysis

To analyze crack widths and locations from the binary image, the crack objects are extracted and grouped based on their longitudinal coordinates. The binary image is first projected to the y axis to create a histogram plot, and the separated histograms are attributed to individual cracks. When two adjacent cracks comprise pixels with overlapped y coordinates, the cracks are separated at the middle point between two histogram peaks. Within the defined range of y coordinates for each crack, the number of pixels was counted to determine the crack width using Eq. (3). The crack location is determined based on the centroid of the objects.

$$w_i = \frac{\sum_{n=1}^{m} A_n}{X} \times Res \qquad (3)$$

where

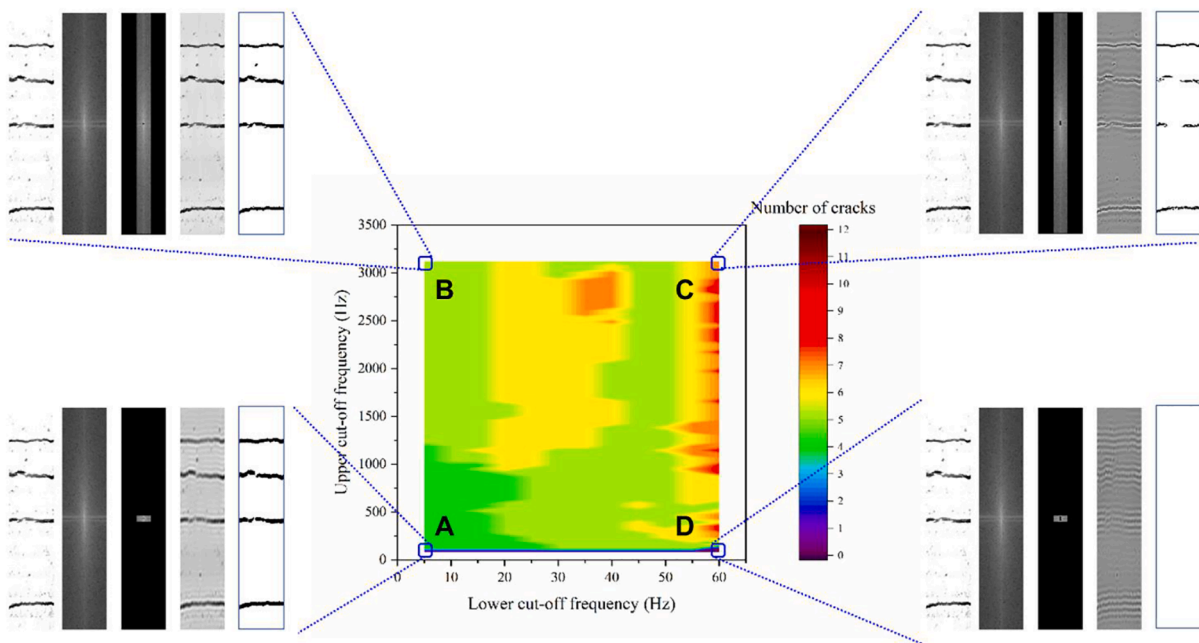w_i is the width of the ith crack

Fig. 11. De-noising effect of upper and lower cut-off frequencies of the bandpass filter.
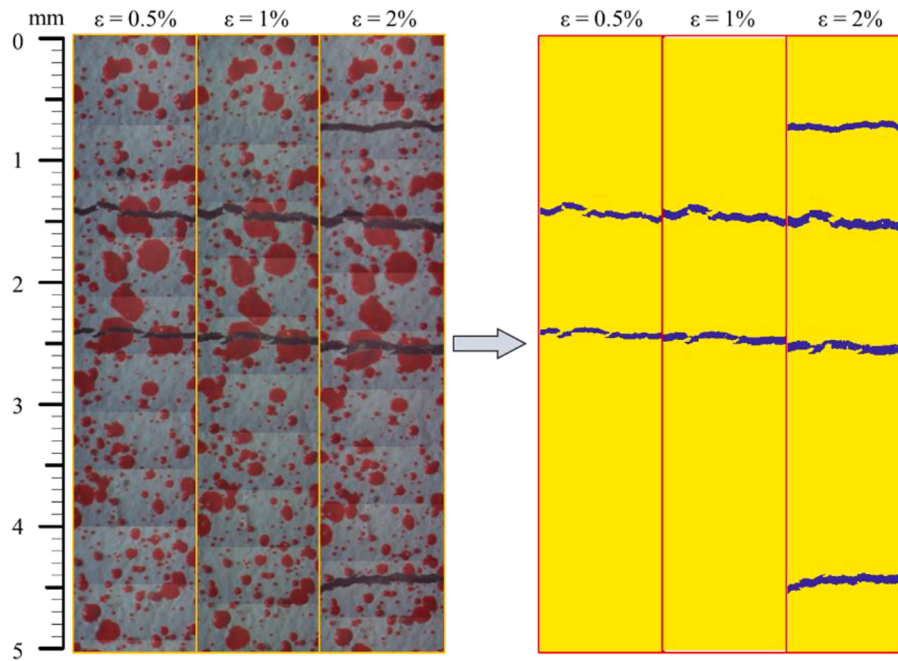
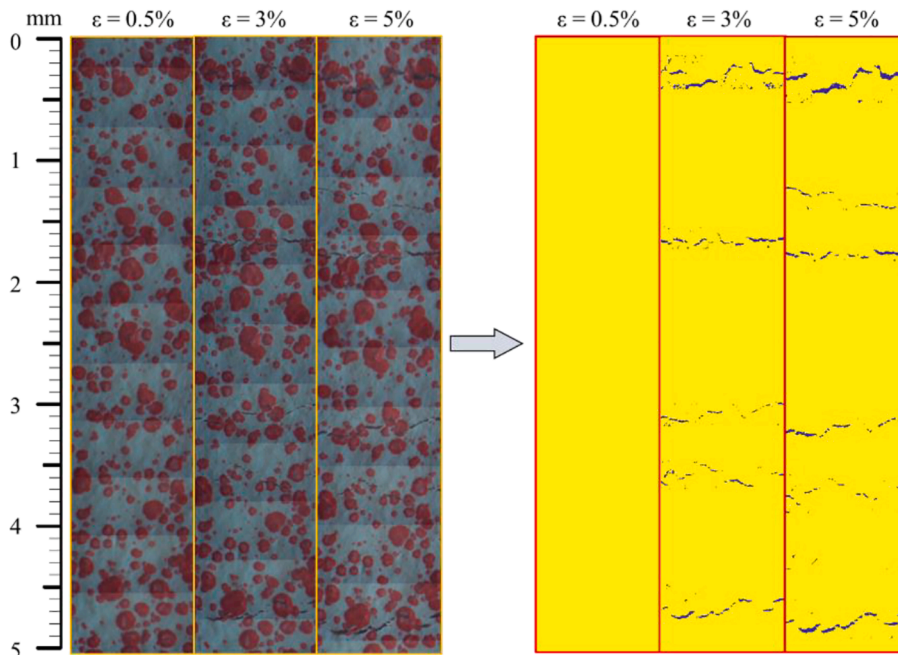**Fig. 12.** Specimen A typical crack patterns of a 5-mm long section at tensile strains of 0.5%, 1%, and 2%.

Fig. 13. Specimen B typical crack patterns of a 5-mm long section at tensile strains of 0.5%, 3%, and 5%.

A_n is the area of the nth object in the ith crack on the binary image, in pixel^2

X is the total length of the $\times$ coordinate projection for each crack, in pixel

Res is the microscope image resolution, in μm/pixel

To complement the system's limited scope of view, DIC is conducted to determine the in-plane deformation and strain distribution along the entire gauge length. The purpose of DIC is to visualize the multiple fine cracks based on the strain concentration and to calculate the crack width distribution as a reference. A commercial software Vic-2D is used. The subset size and step size are chosen as 51 pixels and 1 pixel, respectively.

The selection of subset/step sizes is critical to the calculation efficiency and spatial resolution. Specifically, the subset size should be sufficiently large to contain multiple speckles for uniqueness but may lose resolution when the subset is too large [29]. Large subsets also increase the calculation time. Here, the subset size was chosen to include at least 5 speckles to ensure accurate tracking of the subset location. As a small step size is conducive to higher strain resolution, it is chosen as 1 pixel to attain a sufficient quantity of DIC data points.

4. Crack width distribution and crack spacing

4.1. Microscopy results

The photogrammetric approach described above proves to be effective in extracting the information of crack widths and locations. Figs. 14 and 15 show the individual crack width and longitudinal location at varying loading stages, where multiple cracks were clearly observed. In contrast to Specimen A, Specimen B incorporated with crumb rubber was found to develop much finer and more saturated cracks. For both specimens, all cracks were found below 100 μm in width, irrespective of the imposed strain. The smallest crack was ~ 3 μm which occupied approximately 2 pixels, indicating a good precision for crack width measurement.

The crack width distribution is shown in Figs. 16 and 17 and the statistics of crack width and spacing are listed in Tables 2 and 3. Increasing the tensile strain was found to promote Specimen A's average crack width slightly, but did not impact the average crack width in Specimen B. As shown in Table 3, the cracks in Specimen B maintained a constant average width of 12 μm when the tensile strain increased from 1% to 4% and slightly increased to 14 μm at 5%. Instead of developing larger cracks, the number of cracks was found to increase, leading to a more saturated crack pattern with small spacing. The accumulated crack width, however, was smaller than the total gauge length elongation measured by LVDT. The discrepancy may stem from the narrow view of the microscope which measures a small distance in the transverse direction (i.e., < 1280 μm), whereas the LVDT assesses the average elongation across the entire section. The elastic tensile strain between adjacent cracks also contributes to the LVDT readings but is not counted as the crack widths by microscopy. This contribution can be estimated from the tensile stress and Young's modulus of elasticity, assuming uniform stress distribution in the uncracked matrix blocks between adjacent cracks. In this study, the estimated elastic strain at peak stress was found to be 0.074–0.075%, corresponding to the average crack width variations of 2.96 μm for Specimen A and 0.82 μm for Specimen B. This impact seems to be small compared to the statistical variability in average crack width shown in Tables 2 and 3.

4.2. DIC strain field

To compare results between microscopy and DIC, sequential images taken by the digital camera were analyzed at tensile strains of 0.5%-2% for Specimen A and 0.5%-5% for Specimen B. Figs. 18 and 19 describe the pattern of the longitudinal strain field at each strain level and the respective specimen surface appearance when approaching the ultimate
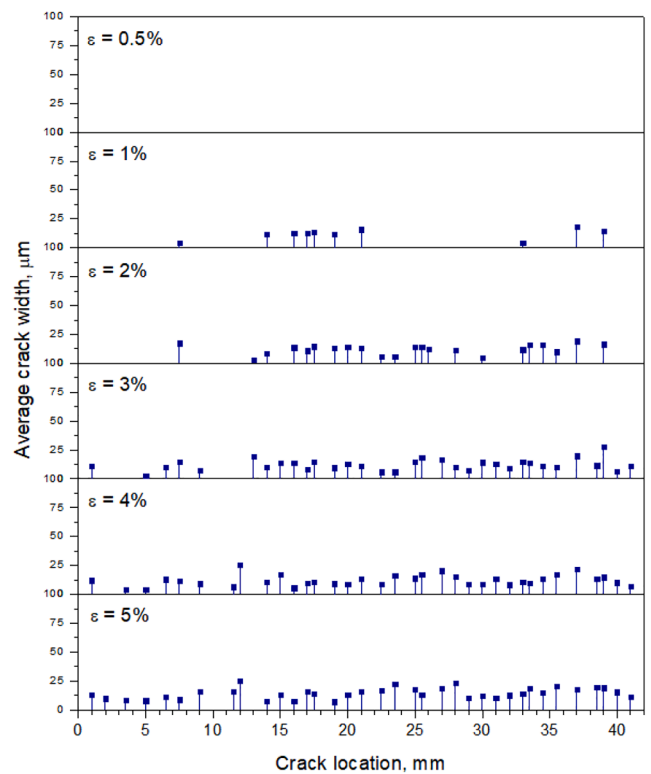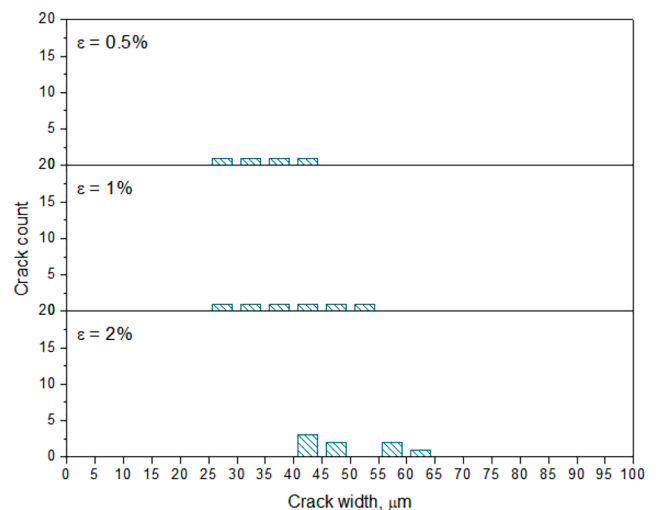

Fig. 15. Specimen B crack width and location.

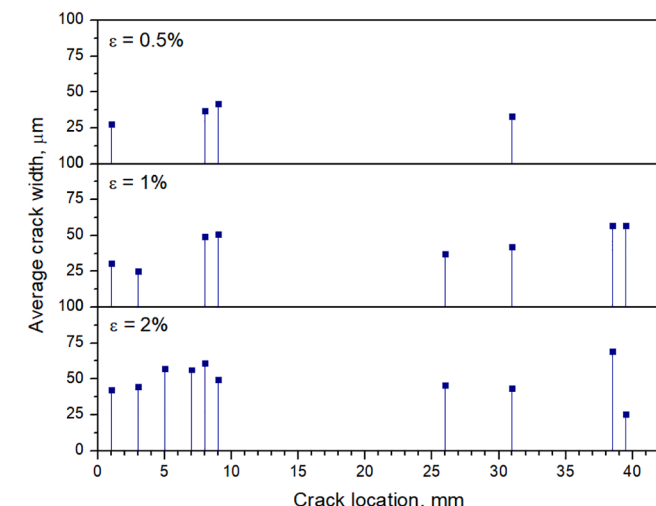Fig. 16. Specimen A crack width distribution.

strain. Along the specimen centerline, the strain data were extracted and plotted against the longitudinal location as shown in Fig. 20. The peaks of strain plots indicate strain concentrations and thus plausible cracks, as the elastic elongation of the uncracked material is orders of magnitude less than cracks. The strain plots exhibit fluctuations and occasionally negative values which were also reported in [16]. The fluctuations were attributed to the material heterogeneity that leads to computational errors in DIC subsets adjacent to cracks. Therefore, the small peaks as part of the fluctuations should not be counted as cracks.

DIC is capable of mapping ECC's crack pattern even when the cracks are tight and invisible to a digital camera or microscope. For Specimen A with relatively large cracks, the DIC strain plot seems to be effective in locating cracks as shown in Fig. 18, and the crack locations visualized on
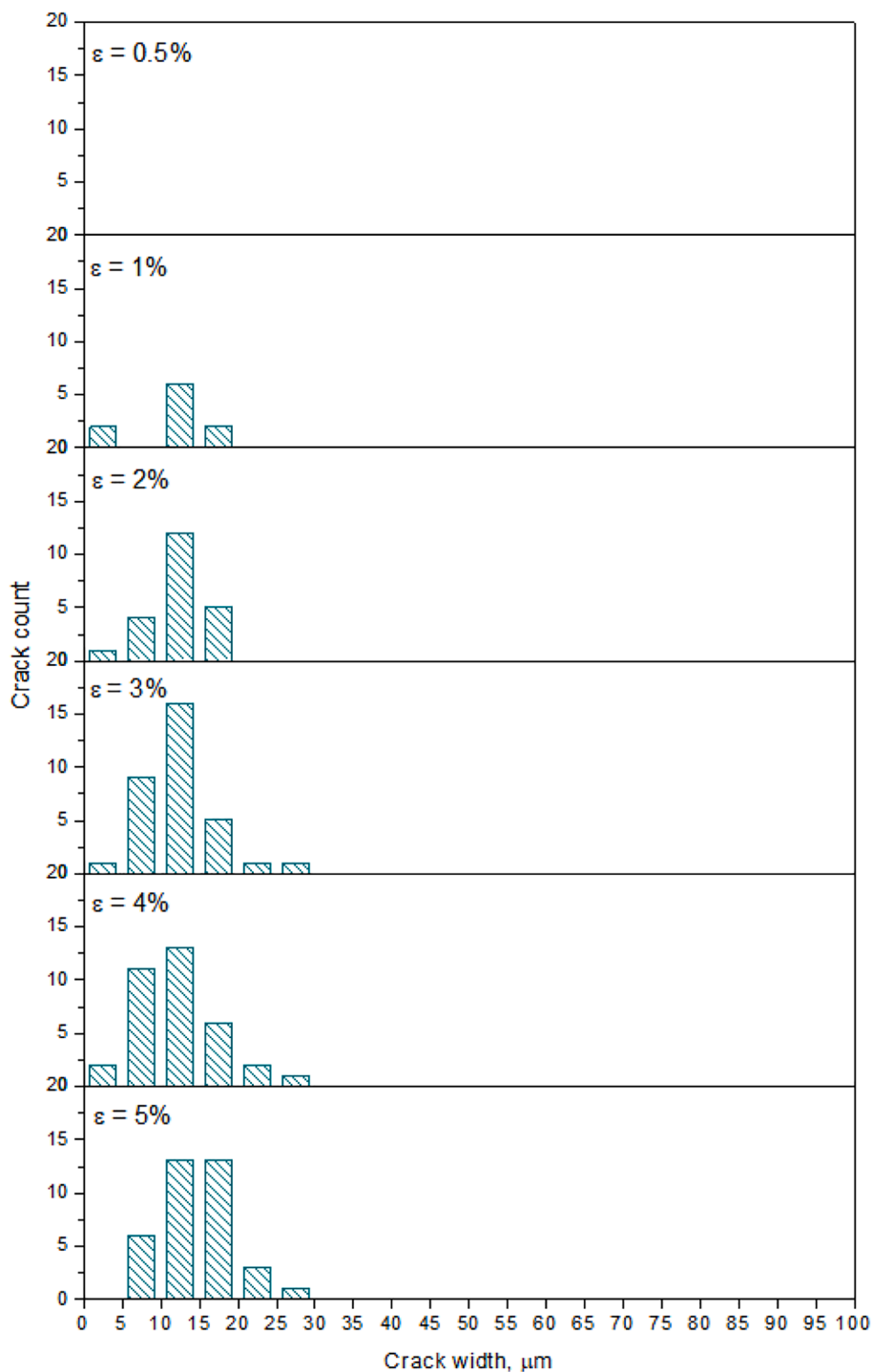

Fig. 14. Specimen A crack width and location.

Fig. 17. Specimen B crack width distribution.

Table 2
Specimen A crack width distribution along centerline by microscopy.

Tensile strain, %	Number of cracks	Maximum crack width, μm	Average crack width, μm	Total crack width, μm	Average crack spacing, mm
0.5	4	42	35 ± 6	140	10.0
1	8	57	44 ± 12	351	5.0
2	10	69	50 ± 12	496	4.0

the specimen surface were found to match the locations of concentrated strains. The strain plots also reveal the multiple cracking process for Specimen B as shown in Fig. 19a–f, indicating possible crack formations in the nearby location. The surface appearance of Specimen B shown in Fig. 19g, however, shows no visible evidence of multiple fine cracks apart from few localized cracks even as the ultimate strain at ~ 5% is approached. The discrepancy between the strain field and surface appearance of Specimen B is attributed to the tight crack width where all cracks were smaller than the image pixel size (~30 μm) as indicated in Fig. 17. The saturated strain concentration pattern in Fig. 19f suggests that sub-pixel cracks can be identified by DIC based on the interpolated

Table 3
Specimen B crack width distribution along centerline by microscopy.

Tensile strain, %	Number of cracks	Maximum crack width, μm	Average crack width, μm	Total crack width, μm	Average crack spacing, mm
0.5	–	–	–	–	–
1	10	18	12 ± 5	119	4.0
2	22	19	12 ± 4	268	1.8
3	33	26	12 ± 5	402	1.2
4	35	27	12 ± 5	422	1.1
5	36	27	14 ± 5	521	1.1

strain values. The crack width distribution is extracted from Fig. 20 and compared with the microscopy results in the following section.

4.3. Comparison of microscopy, DIC, and gauge length elongations for crack width measurement

Compared to the results of direct crack measurement via microscopy, DIC was found to overestimate the crack width and underestimate the number of cracks, especially at high tensile strains. Figs. 21 and 22 compare the results of average crack width and crack number obtained from microscopy, DIC, and/or LVDT. As shown in Fig. 21, the microscopy reported a relatively narrow range of crack width compared to DIC for both specimens. The average crack width is found to be smaller by microscopy than by DIC at all strain levels. For Specimen B with an average crack width of 12–14 μm, DIC reported nearly three times higher results attaining 34–50 μm. DIC was also found to underestimate the number of cracks due to a limited image resolution as well as the tight crack width and crack spacing in Specimen B (see Fig. 20b). As shown in Fig. 22, DIC identified fewer cracks than microscopy for all data points except at a 0.5% tensile strain for Specimen B, in which

cracks were detected by the DIC-computed strain concentrations but invisible under the microscope. As the microscope has a narrow transverse view, DIC seems to outperform microscopy in locating cracks across the entire specimen surface and predicting crack locations before their visible occurrence. Nevertheless, the major disadvantage of DIC lies in the uncertain accuracy of crack width measurement which is dominated by the image resolution in relation to the actual crack width/spacing. A prior study by Ohno and Li [16] attributed the DIC-computed crack width smaller than 20 μm to noises and did not count them as true cracks. Tekieli et al. [17] also indicated that the DIC strain values are unreliable within cracks, thus may lead to an inaccurate crack width calculation from the strain integration. These findings align with the result of this study and suggest that a high image resolution is critical to attaining accurate crack widths with DIC. To overcome resolution limitations, combing microscopy and DIC seems to be a viable approach.

The gauge length elongation measured by LVDT was divided by the total crack number determined by microscopy to estimate the average crack width as shown in Fig. 21. As the tensile strain increases, the average crack width showed a consistently increasing trend for the LVDT elongation and DIC/microscopy. The LVDT elongation, however, tended to overestimate the average crack width compared to microscopy. This is attributed to the limited transverse view of the microscope which reflects cracks only in the vicinity of the specimen centerline rather than the entire surface. The discrepancy in the average crack widths between LVDT and microscopy enlarges for Specimen B, in which the crack number along the centerline is less representative of the full-field cracks due to the crack discontinuity as indicated in Fig. 13. It is suggested that the accuracy of using elongation for estimating the average crack width depends on how the crack number is counted and may lead to uncertain results when cracks are tight and discontinuous.

Table 4 compares the techniques of DIC, microscopy, and gauge length elongation and summarizes their advantages and recommended applications for crack width measurements. Microscopy measures crack
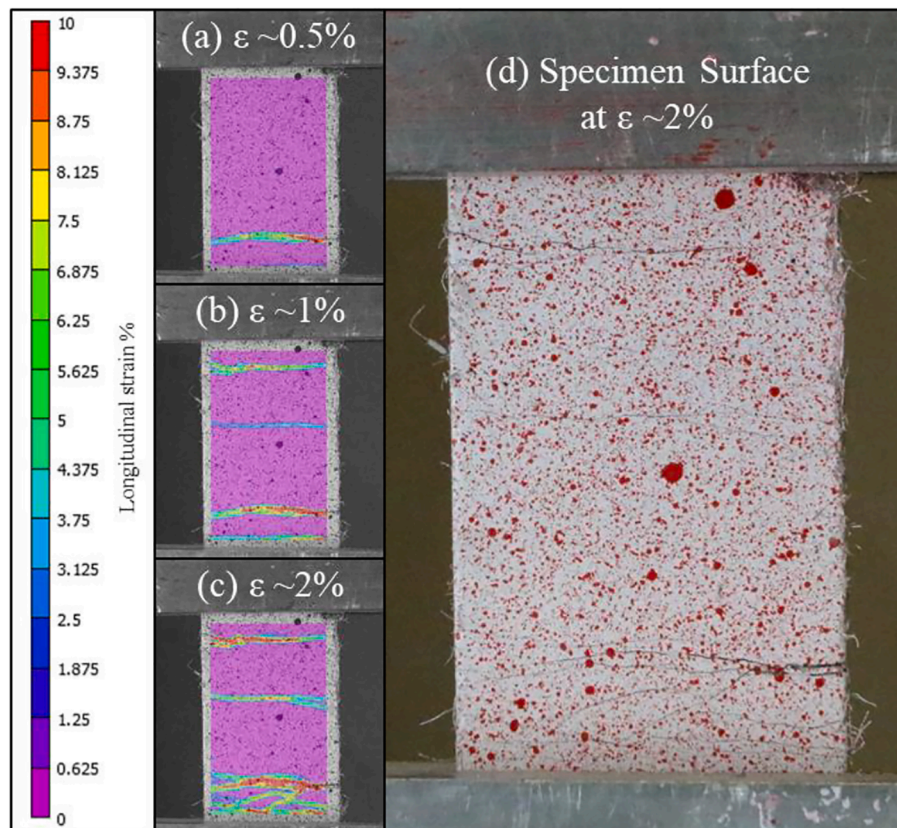
Fig. 18. DIC-computed strain field of Specimen A: (a–c) at 0.5–2% tensile strains, and (d) specimen surface at 2% tensile strain.
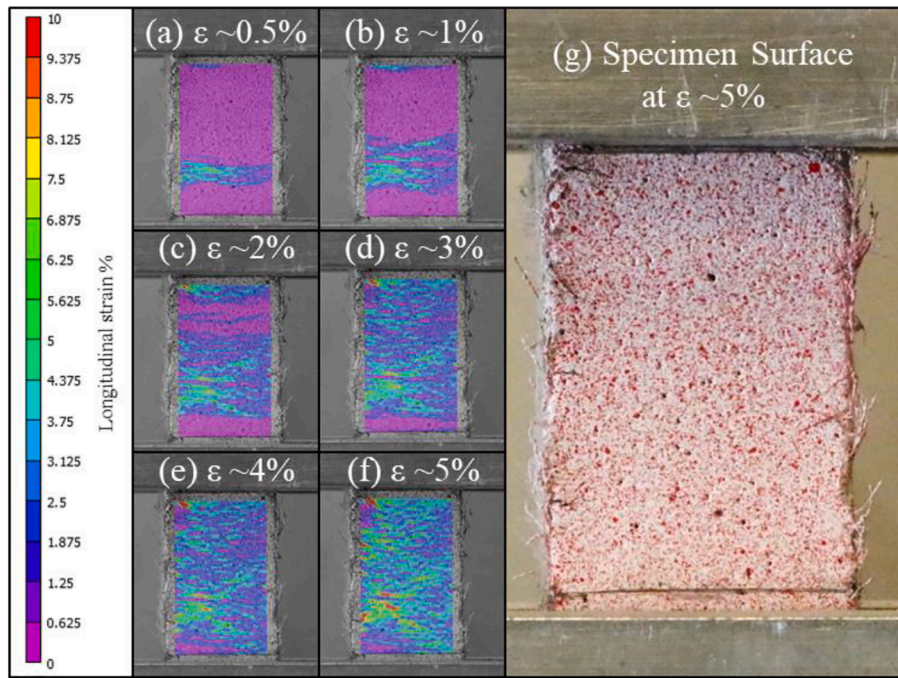
Fig. 19. DIC-computed strain field of Specimen B: (a–f) at 0.5–5% tensile strains, and (g) specimen surface at 5% tensile strain.
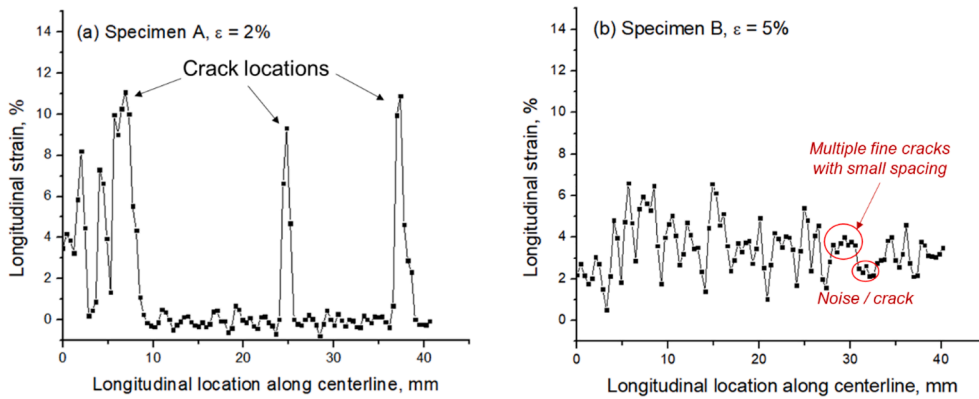

Fig. 20. DIC strain distribution along centerlines of (a) Specimen A, and (b) Specimen B.
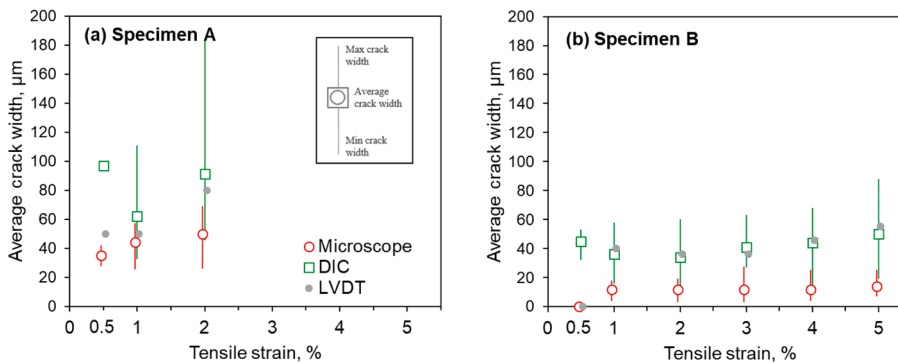

Fig. 21. Average crack width obtained from microscopy, DIC, and LVDT for (a) Specimen A and (b) Specimen B.

width directly, thus producing the most reliable results within the microscopic view. By conducting line scanning and photogrammetric analysis, the microscopy provides accurate information of crack width distribution, location, and spacing, as well as high-resolution visuals of

crack openings. Its major disadvantage is the limited transverse view that leads the technique close to a one-dimensional crack scanning rather than the surface mapping provided by DIC. As an indirect method, DIC effectively captures locations of strain concentration from the strain
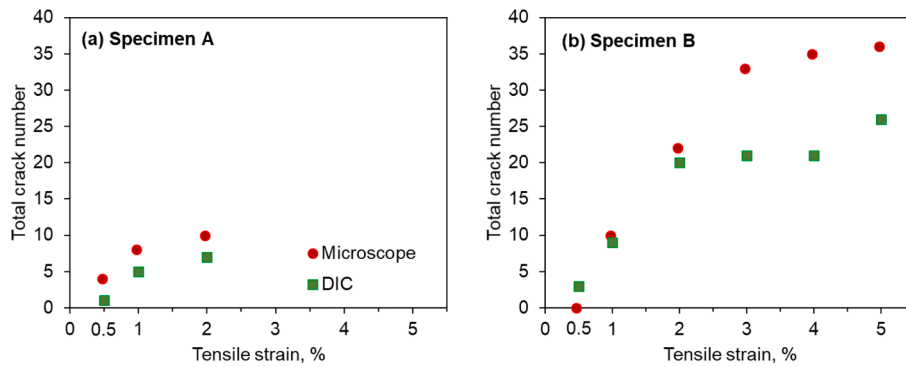
Fig. 22. Crack number obtained from microscopy, DIC, and LVDT for (a) Specimen A and (b) Specimen B.

Table 4
Comparison of microscopy, DIC and gauge length elongation for crack measurement.

Methods	Crack width	Crack number counting	Advantages	Recommendations for application
Microscopy	provide crack location and crack width distribution along a defined line; accurate in visualizing micro-cracks and measuring crack width on material surface	accurate but in a narrow transverse view	high resolution and accuracy; direct crack visuals	for materials with ultrafine crack width (<20 μm); recommend combining DIC for general materials
DIC	provide full-field crack width distribution of entire specimen surface or along any defined line; may overestimate average crack width and overlook sub-pixel fine cracks	undercount the number of tight cracks with small crack spacing	provide 2D (and 3D) strain distribution; predict crack formation based on strain concentration	for general measurement in case of sufficient image resolution compared to actual crack width; otherwise recommended for combining with microscopy
Gauge length elongation	provide average crack width of entire specimen; may overestimate average crack width; o crack width distribution	need additional inputs of crack number	easy to operate; no additional hardware/software needed	for initial and quick estimate

contour map and can identify fine cracks before their visible occurrence under the microscope. When integrating the strain values for crack width, however, DIC is subjected to computational errors and demands high image resolutions relative to the actual crack width/spacing. For cracks smaller than 10–20 μm, DIC tends to overestimate crack widths when using regular digital cameras and is recommended to combine the microscopy for crack width measurement. Dividing the elongation by crack number as an indirect but easy-to-operate method provides the average crack width only and can be used for preliminary estimates. For materials dominated by ultrafine and sub-pixel cracks (such as Specimen B in this study), both DIC and LVDT provide conservative estimates of the average crack width, while DIC results are more insightful owing to the surface strain distribution. In these scenarios, microscopy is recommended for analyzing crack widths at high accuracy.

5. Conclusions

This study proposes a high resolution approach for measuring ECC's multiple fine cracks through optical microscopic line scanning and photogrammetric analysis of specimens during tensioning in a load frame. Conclusions are drawn as follows.

- The proposed scanning microscopy approach provides magnified crack images and delivers accurate measurement of crack locations and crack width distribution on the specimen surface while in loaded condition. With a portable optical microscope, the image resolution can achieve 1.6 μm/pixel (potentially down to 0.3 μm/pixel, thus sensitive to cracks as small as 0.3 μm in width, depending on the microscope model and image acquisition software) at a much lower equipment cost than traditional digital cameras of the same resolution.
- Compared to DIC, microscopy is effective in characterizing ultrafine cracks (e.g., < 30 μm in width) and provides accurate results of crack number and width. However, the narrow transverse view of microscopes limits the crack characterization close to one dimension (i.e.,

line scanning) as opposed to the two-dimensional crack mapping by DIC. This may incur variabilities of the microscopic results among different scan lines.
- DIC is efficient in attaining spatial strain distribution and predicting crack occurrence before the cracks become visible on the specimen surface. When the crack spacing and width are small, however, DIC tends to overestimate the average crack width and undercount the number of fine cracks. While improving the digital image resolution can enhance the accuracy, it is recommended to combine DIC and microscopy for crack measurement, particularly when a significant number of cracks are below the DIC image resolution.
- The photogrammetric technique is designed for lab-scale experimentation and may be extended to the field. Crack images acquired on field structures by remote cameras or microscopes equipped onto a drone or robotic arm can be analyzed in a similar modality. As a surface measurement, the optical microscopy technique can be further combined with techniques such as ultrasonic emission and X-ray computed tomography for 3D characterization of crack depths.

The proposed microscopy technique may be extended to analyzing crack pattern development, specifically in relation to band formation, crack shielding, and other phenomena that might be associated with fiber dispersion and flaw size distribution non-uniformity. Further investigations may enhance the microscope's measuring range via 2-D mapping and increase the speed of image acquisition. The frequency-based de-noising approach warrants additional investigations in refining the selection of cut-off frequencies, which may serve as additional training datasets to enhance the accuracy of machine learning in characterizing micro-cracks.

CRediT authorship contribution statement

Duo Zhang: Conceptualization, Data curation, Formal analysis, Investigation, Methodology, Writing – original draft, Writing – review & editing. **Wentao Wang:** Data curation, Formal analysis, Investigation,

Methodology, Writing – original draft. **Victor C. Li:** Conceptualization, Project administration, Resources, Supervision, Writing – review & editing.

Declaration of Competing Interest

The authors declare that they have no known competing financial interests or personal relationships that could have appeared to influence the work reported in this paper.

Acknowledgment

References

[1] M.D. Lepech, V.C. Li, Water permeability of engineered cementitious composites, Cem. Concr. Compos. 31 (10) (2009) 744–753.

[2] M. Sahmaran, M. Li, V.C. Li, Transport properties of engineered cementitious composites under chloride exposure, ACI Mater. J. 104 (6) (2007) 604.

[3] M. Şahmaran, İ.Ö. Yaman, Influence of transverse crack width on reinforcement corrosion initiation and propagation in mortar beams, Can. J. Civ. Eng. 35 (3) (2008) 236–245.

[4] Li, V.C., Engineered Cementitious Composites (ECC): Bendable Concrete for Sustainable and Resilient Infrastructure. 2019: Springer.

[5] Li, V.C., Engineered cementitious composites (ECC) material, structural, and durability performance. 2008.

[6] V.C. Li, On engineered cementitious composites (ECC). A review of the material and its applications, J. Adv. Concr. Technol. 1 (3) (2003) 215–230.

[7] V.C. Li, Engineered cementitious composites (ECC) – Tailored composites through micromechanical modeling, in: N. Banthia, A. Bentur, A.A. Mufti (Eds.), Fiber Reinforced Concrete Present and Future, Canadian Society for Civil Engineering, Montreal (Canada), 1997, pp. 64–97.

[8] V.C. Li, S. Wang, C. Wu, Tensile strain-hardening behavior of polyvinyl alcohol engineered cementitious composite (PVA-ECC), ACI Mater. J. Am. Concr. Inst. 98 (6) (2001) 483–492.

[9] S. Wang, V.C. Li, Engineered cementitious composites with high-volume fly ash, ACI Mater. J. 104 (3) (2007) 233.

[10] H. Liu, Q. Zhang, C. Gu, H. Su, V. Li, Self-healing of microcracks in engineered cementitious composites under sulfate and chloride environment, Constr. Build. Mater. 153 (2017) 948–956.

[11] L.-L. Kan, et al., Self-healing characterization of engineered cementitious composite materials, ACI Mater. J. 107 (6) (2010).

[12] D. Zhang, et al., Autogenous healing of engineered cementitious composites (ECC) based on MgO-fly ash binary system activated by carbonation curing, Constr. Build. Mater. 238 (2020), 117672.

[13] E.-H. Yang, Y. Yang, V.C. Li, Use of high volumes of fly ash to improve ECC mechanical properties and material greenness, ACI Mater. J. 104 (6) (2007) 620.

[14] J. Zhou, S. Qian, M.G. Sierra Beltran, G. Ye, K. van Breugel, V.C. Li, Development of engineered cementitious composites with limestone powder and blast furnace slag, Mater. Struct. 43 (6) (2010) 803–814.

[15] J.-I. Choi, B.Y. Lee, R. Ranade, V.C. Li, Y. Lee, Ultra-high-ductile behavior of a polyethylene fiber-reinforced alkali-activated slag-based composite, Cem. Concr. Compos. 70 (2016) 153–158.

[16] M. Ohno, V.C. Li, A feasibility study of strain hardening fiber reinforced fly ash-based geopolymer composites, Constr. Build. Mater. 57 (2014) 163–168.

[17] M. Tekieli, S. De Santis, G. de Felice, A. Kwiecień, F. Roscini, Application of digital image correlation to composite reinforcements testing, Compos. Struct. 160 (2017) 670–688.

[18] W. Peters, W. Ranson, Digital imaging techniques in experimental stress analysis, Opt. Eng. 21 (3) (1982), 213427.

[19] F. Abbassi, F. Ahmad, Behavior analysis of concrete with recycled tire rubber as aggregate using 3D-digital image correlation, J. Cleaner Prod. 274 (2020), 123074.

[20] S.-W. Khoo, S. Karuppanan, C.-S. Tan, A review of surface deformation and strain measurement using two-dimensional digital image correlation, Metrol. Measure. Syst. 23 (3) (2016) 461–480.

[21] G.P.A.G. van Zijl, V. Slowik, R.D. Toledo Filho, F.H. Wittmann, H. Mihashi, Comparative testing of crack formation in strain-hardening cement-based composites (SHCC), Mater. Struct. 49 (4) (2016) 1175–1189.

[22] H. Liu, Q. Zhang, C. Gu, H. Su, V.C. Li, Influence of micro-cracking on the permeability of engineered cementitious composites, Cem. Concr. Compos. 72 (2016) 104–113.

[23] H. Liu, Q. Zhang, C. Gu, H. Su, V. Li, Influence of microcrack self-healing behavior on the permeability of Engineered Cementitious Composites, Cem. Concr. Compos. 82 (2017) 14–22.

[24] Brigham, E.O., The fast Fourier transform and its applications. 1988: Prentice-Hall, Inc.

[25] Van Loan, C., Computational frameworks for the fast Fourier transform. 1992: SIAM.

[26] Bracewell, R.N. and R.N. Bracewell, The Fourier transform and its applications. Vol. 31999. 1986: McGraw-Hill New York.

[27] Rao, K.R., D.N. Kim, and J.J. Hwang, Fast Fourier transform: algorithms and applications. 2010.

[28] Smith, S., Digital signal processing: a practical guide for engineers and scientists. 2013: Elsevier.

[29] Sutton, M.A., J.J. Orteu, and H. Schreier, Image correlation for shape, motion and deformation measurements: basic concepts, theory and applications. 2009: Springer Science & Business Media.